



**HAL**  
open science

## Some new applications of a second-gradient model for porous ductile materials

Jun Yang, Rémi Lacroix, Jean-Michel Bergheau, Jean-Baptiste Leblond,  
Fanny Mas

### ► To cite this version:

Jun Yang, Rémi Lacroix, Jean-Michel Bergheau, Jean-Baptiste Leblond, Fanny Mas. Some new applications of a second-gradient model for porous ductile materials. *European Journal of Mechanics - A/Solids*, 2019, 76, pp.180-192. 10.1016/j.euromechsol.2019.03.013 . hal-02285366

**HAL Id: hal-02285366**

**<https://hal.sorbonne-universite.fr/hal-02285366>**

Submitted on 12 Sep 2019

**HAL** is a multi-disciplinary open access archive for the deposit and dissemination of scientific research documents, whether they are published or not. The documents may come from teaching and research institutions in France or abroad, or from public or private research centers.

L'archive ouverte pluridisciplinaire **HAL**, est destinée au dépôt et à la diffusion de documents scientifiques de niveau recherche, publiés ou non, émanant des établissements d'enseignement et de recherche français ou étrangers, des laboratoires publics ou privés.

# Some new applications of a second-gradient model for porous ductile materials

★

Jun Yang<sup>1</sup>, Rémi Lacroix<sup>1</sup>, Jean-Michel Bergheau<sup>2</sup>,  
Jean-Baptiste Leblond<sup>3\*</sup>, Fanny Mas<sup>4</sup>

<sup>1</sup>*ESI-France, Le Récamier, 70 rue Robert, 69006 Lyon, France*

<sup>2</sup>*Université de Lyon, ENISE, CNRS, UMR 5513, LTDS, 58 rue Jean Parot, 42023  
Saint-Etienne Cedex 02, France*

<sup>3</sup>*Sorbonne Université, Faculté des Sciences et Ingénierie, Campus Pierre et Marie Curie,  
CNRS, UMR 7190, Institut Jean Le Rond d'Alembert, 75252 Paris Cedex 05, France*

<sup>4</sup>*Grenoble INP, CNRS, UMR 5266, SIMaP, 1130 rue de la Piscine, Domaine Universitaire,  
38402 Saint Martin d'Herès Cedex, France*

---

## Abstract

A second-gradient model for porous ductile materials extending the standard GTN first-gradient model (Gurson, 1977; Tvergaard, 1981; Tvergaard and Needleman, 1984) was proposed by Gologanu *et al.* (1997), with the aim of solving the problem of potentially unlimited localization of strain and damage resulting in mesh sensitivity in finite element computations. An efficient numerical implementation of Gologanu *et al.* (1997)'s model has been proposed by Bergheau *et al.* (2014), using an innovative procedure of elimination of the additional nodal degrees of freedom representing the strains (“nodal strains”). The aim of this paper is to present some new applications of the model and associated numerical algorithm. The first, relatively simple application consists of 2D numerical simulations of an experiment of ductile rupture of some pre-notched and pre-cracked CT specimen. The goal here is essentially to illustrate one major advantage of the procedure of elimination of the nodal strains, the possibility of easily mixing elements obeying first- and second-gradient models, and thus using the latter type of model only in those limited zones where it is really needed. The second, more complex application, concerns the 3D numerical simulation of crack propagation over a long distance in a multiphase material. The aim here is to illustrate the possibility of using the model, in spite of its sophistication, for the study of complex fracture problems of practical, industrial interest.

### *Key words:*

Porous ductile solids, second-gradient model, numerical implementation, mix of first- and second-gradient models, simulation of rupture tests

---

\* This article was presented at the IUTAM Symposium on Size-Effects in Microstructure and Damage Evolution at the Technical University of Denmark, 2018.

\* Corresponding author.

## 1 Introduction

The standard GTN first-gradient model (Gurson, 1977; Tvergaard, 1981; Tvergaard and Needleman, 1984) for porous ductile materials involves some softening due to the gradual increase of the porosity. As such, it unfortunately predicts potentially unlimited localization of strain and damage, which entails mesh-dependent results in finite element (FE) computations. Various heuristic, relatively simple solutions have been proposed to settle this issue, see for instance Leblond *et al.* (1994)'s proposal - studied in detail by Enakoutsa *et al.* (2007) - to smooth out spatial variations of the porosity rate by convoluting it with some material-dependent "weighing function". But a more theoretically satisfying - albeit admittedly more complex - solution was proposed by Gologanu *et al.* (1997), in the form of a second-gradient extension of the GTN model. Unlike previous heuristic proposals, that of Gologanu *et al.* (1997) was grounded in micromechanics, since it relied on an extension of Gurson (1977)'s approximate homogenization of a hollow sphere subjected to conditions of *homogeneous* boundary strain rate (Mandel, 1964; Hill, 1967), to conditions of *inhomogeneous* boundary strain rate. The physical idea was to account in this way for possible quick variations of the macroscopic mechanical fields, at the scale of the void spacing, resulting from gradual concentration of the strain in damaged zones.

An efficient FE implementation of Gologanu *et al.* (1997)'s model has recently been proposed by Bergheau *et al.* (2014). An important novelty of this implementation consisted in eliminating the nodal Degrees Of Freedom (DOFs) representing the strains. Such "nodal strains" are classically introduced in numerical implementations of second-gradient models, in order to deduce the strain gradients from them using the first derivatives of the shape functions, rather than from the nodal displacements using the second derivatives of the shape functions. Their elimination leads to a system of equations involving only the nodal displacements. Major advantages of the method include the reduction of the number of unknowns in the system to be solved - 2 displacements per node instead of 2 displacements plus 4 strains in 2D, 3 displacements instead of 3 displacements plus 6 strains in 3D - and an easier convergence of global elastoplastic iterations.

Some first applications of the model and its numerical implementation have been carried out by Bergheau *et al.* (2014), with the following positive conclusions:

- Convergence of the global elastoplastic iterations can be achieved, although it becomes increasingly difficult in case of important damage.
- Numerical results are essentially mesh-independent, which shows that the introduction of second-gradient effects does fulfill the task it was assigned.
- A good agreement of numerical predictions and experimental observations can be obtained for the ductile rupture of typical specimens; more, this can be achieved for a realistic choice of parameters depicting void coalescence, unlike what occurs when the GTN model is used.

The aim of this paper is to present some new applications of Gologanu *et al.* (1997)'s second-gradient extension of the GTN model and Bergheau *et al.* (2014)'s associated numerical implementation, in order to illustrate two aspects:

- The procedure of elimination of the nodal strains permits to mix in a completely straightforward manner elements obeying first- and second-gradient models. This possibility is appealing in that it permits to use the second-gradient model only in the limited, highly damaged zone where it is really needed, thus facilitating convergence of the elastoplastic iterations and lowering the computation time and cost.
- In spite of its complexity, the model and associated numerical algorithm permit full 3D simulations of crack propagation in ductile materials in complicated situations of practical, industrial interest, with “reasonable” rate of convergence of the elastoplastic iterations and computation time.

It is worth noting that the first advantage here is not tied to Gologanu *et al.* (1997)’s specific model but potentially applies to *any* second-gradient model, provided its numerical implementation includes Bergheau *et al.* (2014)’s procedure of elimination of nodal strains.

The paper is organized as follows:

- Section 2 first presents Gologanu *et al.* (1997)’s second-gradient model and Bergheau *et al.* (2014)’s associated numerical algorithm. This exposition is provided to ease the reading of the paper but limited to essential aspects useful in the present context, since detailed presentations have already been given elsewhere (Enakoutsu and Leblond, 2009; Bergheau *et al.*, 2014).
- Section 3 presents some 2D simulations of an experiment of ductile rupture of a CT specimen, including a “reference” computation assuming the whole structure to obey Gologanu *et al.* (1997)’s second-gradient model, plus several computations ascribing such a type of behaviour only to limited zones of various sizes around the propagating crack.
- Section 4 finally presents some full 3D simulations of crack propagation over a long distance in a specimen mimicking a dissimilar metal weld encountered in the nuclear industry, having a complex metallurgical structure.

## 2 A second-gradient model for porous ductile solids and its numerical implementation

### 2.1 Gologanu *et al.* (1997)’s model

The model accounts for large displacements and strains, using a Eulerian setting. The description of internal forces involves Cauchy’s customary stress tensor  $\boldsymbol{\sigma}$ , plus some third-rank “moment” tensor  $\mathbf{m}$  symmetric in its first two indices. This description is summarized in the following expression of the virtual power  $\mathcal{P}^{(i)}$  of internal forces:

$$\mathcal{P}^{(i)} \equiv - \int_{\Omega} \left[ \boldsymbol{\sigma}(\mathbf{x}) : \mathbf{d}(\mathbf{x}) + \mathbf{m}(\mathbf{x}) : \nabla \mathbf{d}(\mathbf{x}) \right] d\Omega = - \int_{\Omega} \left[ \sigma_{ij}(\mathbf{x}) d_{ij}(\mathbf{x}) + m_{ijk}(\mathbf{x}) \frac{\partial d_{ij}}{\partial x_k}(\mathbf{x}) \right] d\Omega. \quad (1)$$

In this equation  $\Omega$  denotes the current domain occupied by the body,  $\mathbf{x}$  the current position-vector, and  $\mathbf{d}(\mathbf{x}) \equiv \frac{1}{2} [(\nabla \mathbf{v})(\mathbf{x}) + (\nabla \mathbf{v})^T(\mathbf{x})]$  ( $d_{ij}(\mathbf{x}) \equiv \frac{1}{2} [\frac{\partial v_i}{\partial x_j}(\mathbf{x}) + \frac{\partial v_j}{\partial x_i}(\mathbf{x})]$ ) the

Eulerian strain rate associated to the virtual velocity field  $\mathbf{v}(\mathbf{x})$ .

The strain rate and its gradient are assumed to be each composed of an elastic and a plastic part:

$$\begin{cases} \mathbf{d} & \equiv \mathbf{d}^e + \mathbf{d}^p \\ \nabla \mathbf{d} & \equiv (\nabla \mathbf{d})^e + (\nabla \mathbf{d})^p, \end{cases} \quad (2)$$

with *a priori* no relation between the quantities  $(\nabla \mathbf{d})^e$  and  $\nabla(\mathbf{d}^e)$ , or  $(\nabla \mathbf{d})^p$  and  $\nabla(\mathbf{d}^p)$ . (The sole existing relation is between  $\mathbf{d}$  and  $\nabla \mathbf{d}$ , the second quantity being the gradient of the first).

The elastic parts of the strain rate and its gradient,  $\mathbf{d}^e$  and  $(\nabla \mathbf{d})^e$ , are assumed to be related through some stiffness tensors to the Jaumann rates of the stress and moment tensors,  $D\boldsymbol{\sigma}/Dt$  and  $D\mathbf{m}/Dt$ , respectively.

The plastic behavior is governed by the following criterion, which stands as an extension of that in the GTN model:

$$\Phi(\boldsymbol{\sigma}, \mathbf{m}, p, \bar{\sigma}) \equiv \frac{1}{\bar{\sigma}^2} \left( \sigma_{eq}^2 + \frac{Q^2}{b^2} \right) + 2p \cosh \left( \frac{3}{2} \frac{\sigma_m}{\bar{\sigma}} \right) - 1 - p^2 \leq 0. \quad (3)$$

In this expression, some elements are exactly the same as in the GTN model:

- $\sigma_{eq} \equiv \left( \frac{3}{2} \boldsymbol{\sigma}' : \boldsymbol{\sigma}' \right)^{1/2}$  ( $\boldsymbol{\sigma}'$ : deviator of  $\boldsymbol{\sigma}$ ) and  $\sigma_m \equiv \frac{1}{3} \text{tr} \boldsymbol{\sigma}$  denote the von Mises equivalent and mean stress;
- the “damage parameter”  $p$  is connected to the porosity (void volume fraction)  $f$  through the relation

$$p \equiv qf^* \quad , \quad f^* \equiv \begin{cases} f & \text{if } f \leq f_c \\ f_c + \delta(f - f_c) & \text{if } f > f_c \end{cases} \quad (4)$$

where  $q$  is *Tvergaard’s parameter* (Tvergaard, 1981),  $f_c$  the *critical porosity at the onset of void coalescence* and  $\delta (> 1)$  a factor describing the accelerated degradation of the material during coalescence (Tvergaard and Needleman, 1984);

- $\bar{\sigma}$  represents some “average yield stress” of the heterogeneous voided matrix.

The following elements, however, are new:

- $Q^2$  is an isotropic quadratic form of the components of  $\mathbf{m}$ , the detailed expression of which - of little importance here - is given in (Gologanu *et al.*, 1997; Enakoutsa and Leblond, 2009; Bergheau *et al.*, 2014);
- $b$  is a “microstructural distance” connected to the mean half-spacing between neighbouring voids.

Both Gurson (1977)’s criterion and its extension by Gologanu *et al.* (1997) were obtained by combining homogenization and limit-analysis; a general result of the second theory is that provided the normality property is obeyed at the local scale, it is preserved in the homogenization process. It follows that the plastic flow rule necessarily obeys this property, which means that the plastic parts of the strain rate and its gradient,  $\mathbf{d}^p$  and

$(\nabla \mathbf{d})^p$ , are connected to the derivatives of the yield function  $\Phi$  with respect to the stress and moment tensors,  $\boldsymbol{\sigma}$  and  $\mathbf{m}$ , through the same and unique positive plastic multiplier.

Finally with regard to the evolutions of the internal parameters, some elements are again the same as in the GTN model:

- the evolution of the porosity  $f$  is still governed by the equation

$$\dot{f} = (1 - f) \text{tr } \mathbf{d}^p \quad (5)$$

resulting from approximate incompressibility of the metallic matrix;

- the “average yield stress”  $\bar{\sigma}$  is still given by

$$\bar{\sigma} \equiv \sigma(\bar{\epsilon}) \quad (6)$$

where  $\sigma(\epsilon)$  denotes the yield stress of the sound material - a function of the equivalent cumulated plastic strain  $\epsilon$  - and  $\bar{\epsilon}$  some “average equivalent strain” of the heterogeneous matrix.

But the evolution of this average strain  $\bar{\epsilon}$  is governed by the new equation

$$(1 - f) \sigma \dot{\bar{\epsilon}} = \boldsymbol{\sigma} : \mathbf{d}^p + \mathbf{m} \dot{:(\nabla \mathbf{d})^p} = \sigma_{ij} d_{ij}^p + m_{ijk} (\nabla d)_{ijk}^p, \quad (7)$$

which stands as an extension of Gurson (1977)’s equation incorporating the extra term  $\mathbf{m} \dot{:(\nabla \mathbf{d})^p} = m_{ijk} (\nabla d)_{ijk}^p$  in the expression of the plastic dissipation.

## 2.2 Numerical implementation - Mix of elements obeying first- and second-gradient models

### 2.2.1 Generalities

We discuss here the problem of getting the values of all variables at some time  $t + \Delta t$  from those at some previous time  $t$  using the FE method, with special emphasis on how to mix elements obeying first- and second-gradient models. Since the algorithm of projection of the elastic predictor onto Gologanu *et al.* (1997)’s yield locus has already been discussed at length by Enakoutsa and Leblond (2009), we do not insist on this specific feature of the model and focus instead on the treatment of the second spatial derivatives of the displacement. It is important to note that this issue arises for *all* second-gradient models, not only that of Gologanu *et al.* (1997), and that similarly the solutions proposed below - including in particular the procedure for mixing elements obeying first- and second-gradient models - potentially apply to all models of this type.

### 2.2.2 Interpolation of the increments of displacement and strain

The increment of displacement  $\Delta \mathbf{u} \equiv \mathbf{v} \Delta t$  between times  $t$  and  $t + \Delta t$  is interpolated using the usual FE scheme:

$$\Delta \mathbf{u}(\mathbf{x}) = \sum_p N^p(\mathbf{x}) \Delta \mathbf{u}^p \quad (8)$$

where  $N^p(\mathbf{x})$  denotes the shape function associated to node  $p$  and  $\Delta \mathbf{u}^p$  the value of  $\Delta \mathbf{u}$  at this node. The components of the increment of strain  $\Delta \boldsymbol{\epsilon} \equiv \mathbf{d} \Delta t \equiv \frac{1}{2} \{ \nabla(\Delta \mathbf{u}) + [\nabla(\Delta \mathbf{u})]^T \}$  are then given by

$$\Delta \epsilon_{ij}(\mathbf{x}) = \sum_p \frac{1}{2} [N_{,j}^p(\mathbf{x}) \Delta u_i^p + N_{,i}^p(\mathbf{x}) \Delta u_j^p]. \quad (9)$$

Similar formulae apply to virtual quantities.

To get the gradient of the increment of strain without differentiating equation (8) twice (an illicit operation for standard elements of class  $\mathcal{C}^0$ ), we introduce an extra tensorial variable  $\Delta \mathbf{w}$  supposedly identical to the increment of strain  $\Delta \boldsymbol{\epsilon}$ . This quantity is interpolated similarly to  $\Delta \mathbf{u}$ :

$$\Delta \mathbf{w}(\mathbf{x}) = \sum_p N^p(\mathbf{x}) \Delta \mathbf{w}^p \quad (10)$$

where  $\Delta \mathbf{w}^p$  denotes the value of  $\Delta \mathbf{w}$  at node  $p$ . The components of the gradient of  $\Delta \mathbf{w}$  follow:

$$\Delta w_{ij,k}(\mathbf{x}) = \sum_p N_{,k}^p(\mathbf{x}) \Delta w_{ij}^p \quad (11)$$

where only first derivatives of shape functions are involved. Again, virtual quantities are interpolated likewise.

### 2.2.3 Enforcement of coincidence of the additional variable and the increment of strain

The algorithm requires enforcing the coincidence of  $\Delta \mathbf{w}$  and  $\Delta \boldsymbol{\epsilon}$ . A simple and efficient way of doing so through some weak formulation has been proposed by Bergheau *et al.* (2014). The output of their procedure, summarized in Appendix A, is a linear equation of the form

$$\Delta \mathbf{W} = \mathbf{A} \cdot \Delta \mathbf{U}, \quad (12)$$

where  $\Delta \mathbf{U}$  and  $\Delta \mathbf{W}$  denote the ‘‘global vectors’’ made from all nodal values of  $\Delta \mathbf{u}$  and  $\Delta \mathbf{w}$ , and  $\mathbf{A}$  a ‘‘global matrix’’ of purely geometrical nature (independent of the constitutive law), which may be obtained through knowledge of the geometry and shape functions.

The matrix  $\mathbf{A}$  must be updated in time since it depends on the current geometry. However this leaves open the choice of updating it only at the beginning of each time-step, using the geometry at time  $t$ , or at each global elastoplastic iteration of each time-step, using the geometry at  $t + \Delta t$ . The choice between these two options cannot be based on considerations of accuracy since both of them involve errors of the same order,  $O((\Delta t)^2)$ . But the second one would require differentiating  $\mathbf{A}$  with respect to  $\Delta \mathbf{U}$  to get the global tangent-matrix, and result in non-symmetry of this matrix. For this reason the first option, update of  $\mathbf{A}$  only at the beginning of each time-step, is selected in this work.

#### 2.2.4 Elimination of nodal strains from the governing equations

The principle of virtual work yields, using the expression (1) of the virtual power of internal forces:

$$\mathbf{R}^u \cdot \delta(\Delta \mathbf{U}) + \mathbf{R}^w \cdot \delta(\Delta \mathbf{W}) = 0 \quad (13)$$

for infinitesimal virtual variations,  $\delta(\Delta \mathbf{U})$  and  $\delta(\Delta \mathbf{W})$ , of the vectors  $\Delta \mathbf{U}$  and  $\Delta \mathbf{W}$ . The quantities  $\mathbf{R}^u$  and  $\mathbf{R}^w$  here are “residues” involving integrals of the local stress and moment tensors; see details in (Bergheau *et al.*, 2014). The variations  $\delta(\Delta \mathbf{U})$  and  $\delta(\Delta \mathbf{W})$  in equation (13) are not independent since the second must be tied to the first through the same matrix  $\mathbf{A}$  as in equation (12). Using the fact that equation (13) must then hold for arbitrary variations  $\delta(\Delta \mathbf{U})$ , one gets the vectorial equation

$$\mathbf{R} \equiv \mathbf{R}^u + \mathbf{A}^T \cdot \mathbf{R}^w = \mathbf{0}. \quad (14)$$

The residues  $\mathbf{R}^u$  and  $\mathbf{R}^w$  are nonlinear functions of the vectors  $\Delta \mathbf{U}$  and  $\Delta \mathbf{W}$  (*via* the local stress and moment tensors), and therefore of the sole vector  $\Delta \mathbf{U}$  by equation (12). The nonlinear system (14) of equations on the components of this vector may be solved using a Newton method with tangent matrix  $\mathbf{K}$  given by

$$\mathbf{K} \equiv \frac{\partial \mathbf{R}}{\partial \Delta \mathbf{U}} = \frac{\partial \mathbf{R}^u}{\partial \Delta \mathbf{U}} + \frac{\partial \mathbf{R}^u}{\partial \Delta \mathbf{W}} \cdot \frac{\partial \Delta \mathbf{W}}{\partial \Delta \mathbf{U}} + \mathbf{A}^T \cdot \left( \frac{\partial \mathbf{R}^w}{\partial \Delta \mathbf{U}} + \frac{\partial \mathbf{R}^w}{\partial \Delta \mathbf{W}} \cdot \frac{\partial \Delta \mathbf{W}}{\partial \Delta \mathbf{U}} \right),$$

that is,

$$\mathbf{K} \equiv \mathbf{K}^{uu} + \mathbf{K}^{uw} \cdot \mathbf{A} + \mathbf{A}^T \cdot \mathbf{K}^{wu} + \mathbf{A}^T \cdot \mathbf{K}^{ww} \cdot \mathbf{A} \quad (15)$$

where

$$\mathbf{K}^{uu} \equiv \frac{\partial \mathbf{R}^u}{\partial \Delta \mathbf{U}} \quad ; \quad \mathbf{K}^{uw} \equiv \frac{\partial \mathbf{R}^u}{\partial \Delta \mathbf{W}} \quad ; \quad \mathbf{K}^{wu} \equiv \frac{\partial \mathbf{R}^w}{\partial \Delta \mathbf{U}} \quad ; \quad \mathbf{K}^{ww} \equiv \frac{\partial \mathbf{R}^w}{\partial \Delta \mathbf{W}}. \quad (16)$$

The detailed expressions of the matrices  $\mathbf{K}^{uu}$ ,  $\mathbf{K}^{uw}$ ,  $\mathbf{K}^{wu}$ ,  $\mathbf{K}^{ww}$  are given in (Bergheau *et al.*, 2014).

#### 2.2.5 Programming aspects - Mix of elements obeying first- and second-gradient models

Figure 1 provides a flow chart of the algorithm for a given time-step. In this figure features specific to second-gradient aspects are painted blue, and features specific to the mix of first- and second-gradient models are painted red.

Prior to the usual loop on global elastoplastic iterations, a “second-gradient-specific” loop on all elements of the structure is necessary to evaluate and assemble their various contributions to the matrix  $\mathbf{A}$  of equation (12). The loop on elastoplastic iterations follows. For each iteration, a second, more usual loop on elements of the structure must be performed in order to evaluate and assemble their contributions to (i) the partial residues  $\mathbf{R}^u$ ,  $\mathbf{R}^w$  and their combination  $\mathbf{R}^u + \mathbf{A}^T \cdot \mathbf{R}^w$ , and (ii) the partial tangent matrices  $\mathbf{K}^{uu}$ ,  $\mathbf{K}^{uw}$ ,  $\mathbf{K}^{wu}$ ,  $\mathbf{K}^{ww}$  and their combination  $\mathbf{K}^{uu} + \mathbf{K}^{uw} \cdot \mathbf{A} + \mathbf{A}^T \cdot \mathbf{K}^{wu} + \mathbf{A}^T \cdot \mathbf{K}^{ww} \cdot \mathbf{A}$ . The residue  $\mathbf{R}^u$  and tangent matrix  $\mathbf{K}^{uu}$  are standard but the residue  $\mathbf{R}^w$  and tangent matrices  $\mathbf{K}^{uw}$ ,  $\mathbf{K}^{wu}$ ,  $\mathbf{K}^{ww}$  are “second-gradient-specific”. The rest of the algorithm, including the convergence test of iterations and the possible repetition of iterations, is standard.

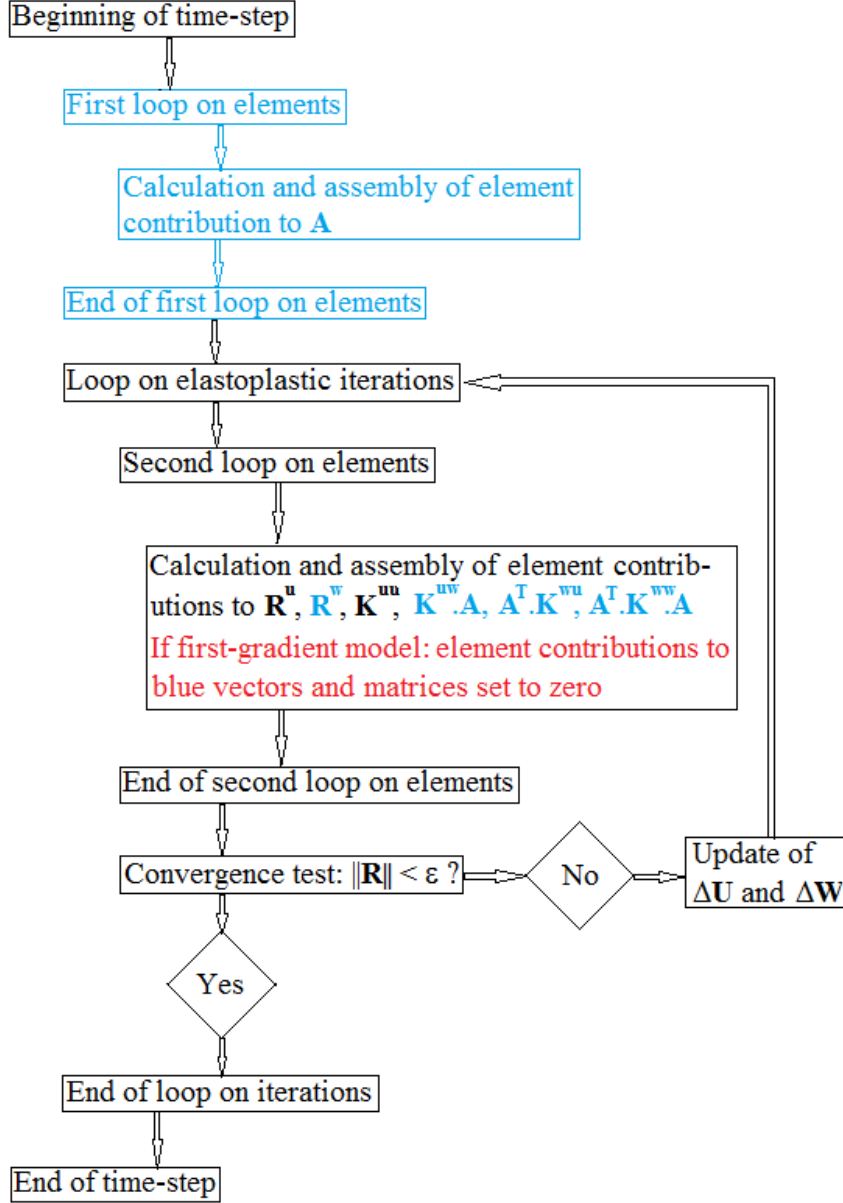


Fig. 1. Flow chart of algorithm for a given time-step. Modifications of the standard algorithm required (i) for second-gradient effects, in blue; (ii) for mix of first- and second-gradients models, in red.

With the algorithm adopted, the mix of elements obeying first- and second-gradient models requires only very minimal adjustments of the programme. Since the nodal DOFs reduce to the sole displacements and are thus the same for the two types of models, no “transition elements” (analogous to those currently used to connect solid elements to beam or plate/shell elements) are necessary; standard meshes may be used, and all features of the programme dealing with geometrical aspects (definition of nodes, elements, shape functions etc.) are strictly unchanged. The first loop on elements of Fig. 1 requires no modification - the matrix  $\mathbf{A}$  must be evaluated using *all* elements, not only those obeying a second-gradient model, in order to avoid inaccuracies in the calculation of the increment of strain  $\Delta \mathbf{w} \equiv \Delta \boldsymbol{\epsilon}$  on the interface between first- and second-gradient zones.

The only necessary adjustments are located in the second loop on elements of Fig. 1, and simply consist in setting the element contributions to the partial residue  $\mathbf{R}^w$  and tangent matrices  $\mathbf{K}^{uw}$ ,  $\mathbf{K}^{wu}$ ,  $\mathbf{K}^{ww}$  to zero in elements satisfying a first-gradient model - since they pertain to the locally non-existent variable  $\Delta \mathbf{w}$ .

Numerical experience shows that the computation time for the second-gradient model may be considerably larger - up to a factor of 10 - than that for the standard first-gradient GTN model. This is due partly to the additional operations required, and partly to the less easily achieved convergence of global elastoplastic iterations. This is why it is essential to limit the use of the second-gradient model to those highly damaged and strained zones where it is really needed.

### 2.2.6 Practical implementation

The algorithm discussed above has been implemented into the SYSTUS<sup>®</sup> finite element software developed by ESI-Group (SYSTUS, 2018). All simulations discussed below have been performed using this software.

## 3 Numerical simulation of ductile rupture of a CT specimen

Some numerical simulations of rupture of a CT specimen performed by Bergheau *et al.* (2014), using Gologanu *et al.* (1997)'s second-gradient model in the whole structure, are supplemented here with new calculations where this model is used only in various vicinities of the crack, the rest of the structure obeying a simple von Mises first-gradient model. The aim is to illustrate the possibility offered by Bergheau *et al.* (2014)'s numerical algorithm to easily mix elements obeying first- and second-gradient models, and the practical efficiency of the procedure. For completeness the results of Bergheau *et al.* (2014)'s original simulations are briefly recalled first.

### 3.1 Presentation of the problem

The problem considered is that of the numerical simulation of fracture tests of CT12 specimens<sup>1</sup> performed by Marie (2000).

The structure and mesh are shown in Fig. 2. Only the right half of the specimen is represented and meshed, thanks to the existence of a vertical plane of symmetry (on the extreme left of the mesh represented in the figure). The width, height and thickness are 25 mm, 25 mm and 12 mm respectively. A 2 mm-deep notch, located on the left boundary of the mesh, runs from the top surface down to a depth of 85 mm. This notch ultimately becomes triangular, with a notch root angle of 60°. A 1.34 mm-deep fatigue pre-crack (invisible in the figure) originates from the root of the notch.

<sup>1</sup> The number refers to the thickness in mm.

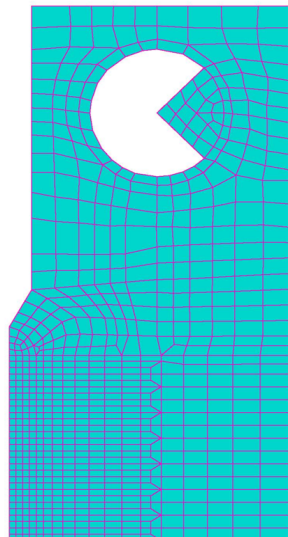


Fig. 2. Mesh of the CT12 specimen.

In Marie (2000)’s experiments, lateral shallow notches ensured approximate plane strain conditions in the region of the crack propagating ahead of the notch. This permits to perform light 2D simulations, with a plane strain hypothesis. To compensate for errors introduced by this hypothesis, when the results of these simulations are compared to experimental observations, the experimental force per unit thickness is slightly corrected by dividing the experimental force applied by an “equivalent thickness” of 10.3 mm (best value determined by Brosse (2009)), differing a bit from the true one of 12 mm.

The issue of mesh sensitivity in simulations using Gologanu *et al.* (1997)’s model has already been studied by Enakoutsa (2007) and Enakoutsa and Leblond (2009), with the conclusion that introduction of second-gradient effects does permit to get numerical results essentially independent of the element size. A single 2D mesh is therefore used.

The specimen is made of SS 316L stainless steel. The material parameters used are provided in Appendix B, including the full uniaxial stress-strain curve. Note that the value of the microstructural distance  $b$  of equation (3) is 0.5 mm, to be compared to the minimum element size (in the region of the crack) of 0.3 mm; the gap between the two is, by our previous numerical experience (Enakoutsa, 2007; Enakoutsa and Leblond, 2009), sufficient to warrant mesh-independent results.<sup>2</sup>

---

<sup>2</sup> The value of  $b$  is probably a bit large, considering the average spacing between neighbouring voids in the material; it is used to as to permit “relatively quick” calculations using a “relatively coarse” mesh. It could certainly be decreased, at the expense of longer calculations and some slight modifications of coalescence parameters.

### 3.2 Simulations using Gologanu *et al.* (1997)'s model in the whole structure

Figure 3<sup>3</sup> displays the experimental load-displacement curve in dark blue, together with several numerical ones:

- In red, a curve obtained with Gologanu *et al.* (1997)'s model, with the coalescence parameters  $f_c = 0.05$ ,  $\delta = 2$ .
- In light blue, a curve obtained with the standard GTN first-gradient model, with the same coalescence parameters.
- In brown, a curve obtained again with Gologanu *et al.* (1997)'s model, but disregarding coalescence.

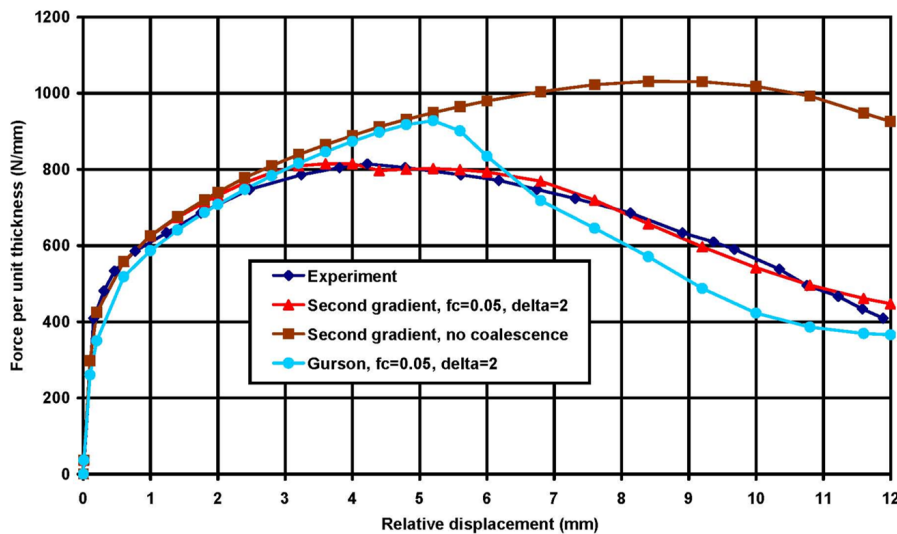


Fig. 3. Comparison of experimental and computed load-displacement curves of the CT12 specimen.

Comparison of these various curves yields the following observations:

- The close agreement between the dark blue experimental curve and the red numerical curve shows that excellent results may be obtained using Gologanu *et al.* (1997)'s model, with relatively high values (a few percent) of the critical porosity  $f_c$  at the onset of coalescence. Such values are compatible with the estimates obtained through FE simulations of elementary porous cells; see the work of Koplik and Needleman (1988) and its many successors.
- On the other hand, the disagreement between the dark blue experimental curve and the light blue numerical curve shows that the same cannot be said of the GTN model. In fact, numerical experience over the years has consistently shown that satisfactorily reproducing the results of ductile fracture experiments using the GTN model requires using small critical porosities  $f_c$  at the onset of coalescence, of the order of one tenth of those predicted by numerical micromechanical simulations. (Another common approach consists of postulating the presence of some additional term representing void nucleation

<sup>3</sup> Although this figure was presented in the work of Bergheau *et al.* (2014), it is included here again because the results are analyzed in more detail.

in the expression of the porosity rate; but as a rule the values of the material parameters appearing in this term have no experimental justification).

- The disagreement between the dark blue experimental curve and the brown numerical curve illustrates the fact that the model must include coalescence in one way or another in order to reproduce experimental results. In other words the predictions of Gologanu *et al.* (1997)'s model are sensitive to the value of  $f_c$ , so that the good quality of results obtained with the high value  $f_c = 0.05$  is not fortuitous but significant.

The fact that to reproduce experimental results, higher (and more realistic) values of  $f_c$  are required for Gologanu *et al.* (1997)'s model than for the GTN model, is an indication that the growth of the porosity is, for given values of the coalescence parameters, quicker for Gologanu *et al.* (1997)'s model. Explaining this phenomenon is not a trivial task, especially so since for values of the opening displacement not exceeding 3 mm, the response of the structure is, on the contrary, (slightly) harder for Gologanu *et al.* (1997)'s model than for the GTN model (see Fig. 3). Although these apparently conflicting observations require further investigations, some preliminary explanations may be found in the following two competing mechanisms:

- Gologanu *et al.* (1997)'s model was originally derived through homogenization over some RVE of finite, fixed volume (of size comparable to the average spacing between neighbouring voids), which means that the strain rate and stress in this model in fact represent *average values* over smaller-scale volumes. This results in a kind of “regularizing effect” (apparent for instance in Enakoutsa and Leblond (2009)'s analytic solution for bending of a plastic beam), which tends to reduce the detrimental effects of geometrical singularities; in other words the model tends to make structures more resistant to such singularities.
- With respect to Gurson (1977)'s yield function, that of Gologanu *et al.* (1997) includes the extra term  $\frac{1}{\sigma^2} \frac{Q^2}{b^2}$ , the effect of which is to lower the magnitude of stress tensors satisfying the criterion. This “second-gradient-induced softening” must result in an increased porosity rate.

In the present example, the first effect probably dominates at the beginning of the loading, because the geometrical singularity at the crack tip is maximum, and the porosity is too small to significantly influence the overall response. But the second effect probably takes over later, because crack blunting reduces the geometrical singularity, and the impact of the much larger porosity upon the overall response becomes important.

Figures 4 and 5 illustrate some interesting features of the numerical solution, for both the GTN model and Gologanu *et al.* (1997)'s model (including coalescence). Figure 4 displays the final distribution - at time  $t = 6$  s - of the porosity on the deformed configuration of the specimen (without any magnification of the displacements), obtained with the GTN model. Figure 5 compares this distribution to that obtained with Gologanu *et al.* (1997)'s model; the comparison being hampered by the fact the development of the porosity does not occur at the same rate for the two models, the porosity distribution for Gologanu *et al.* (1997)'s model is shown at two instants,  $t = 4.8$  s corresponding to the same crack advance as in Fig. 4 for the GTN model, and  $t = 6$  s corresponding to the same loading level.

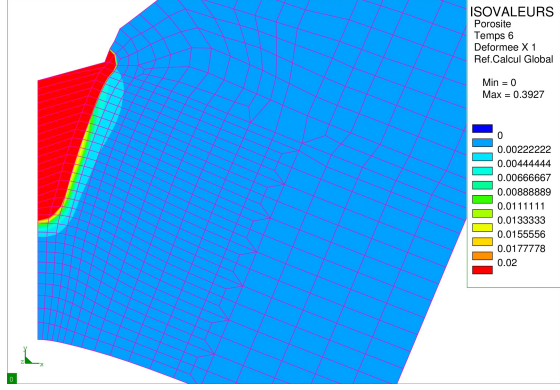
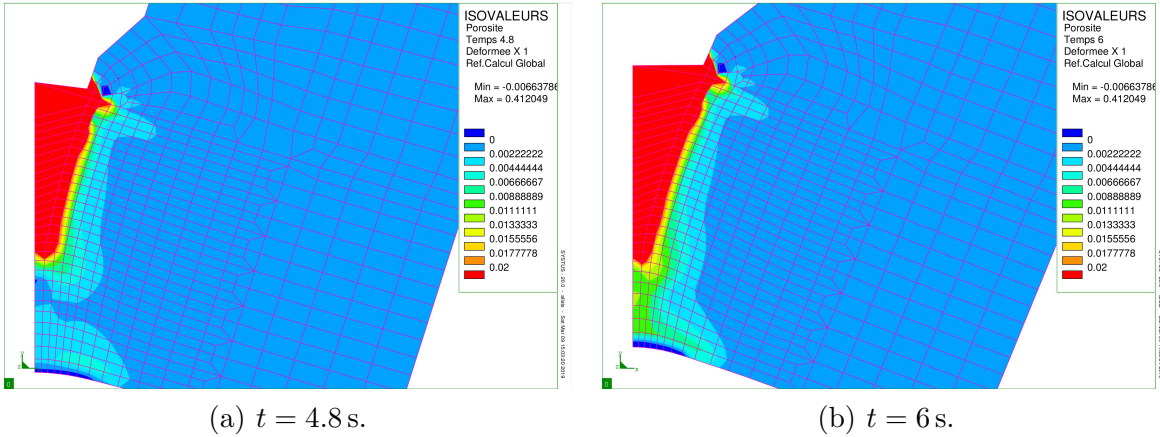


Fig. 4. Distribution of porosity at time  $t = 6$  s in the CT12 specimen - GTN model.



(a)  $t = 4.8$  s.

(b)  $t = 6$  s.

Fig. 5. Distribution of porosity at times  $t = 4.8$  and  $6$  s in the CT12 specimen - Gologanu *et al.* (1997)'s model.

Comparison of Figs. 4 and 5(b) shows that for a given loading level, the development of the porosity is more important for Gologanu *et al.* (1997)'s model than for the GTN model, which confirms the existence of the second mechanism suggested above. Comparison of Figs. 4 and 5(a) shows that for a given stage of crack propagation, Gologanu *et al.* (1997)'s model predicts a slightly more spread distribution of porosity than the GTN model, confirming the expected limitation of the concentration of damage resulting from introduction of second-gradient effects.

### 3.3 Simulations using a mix of elements obeying first- and second-gradient models

We now restrict the use of Gologanu *et al.* (1997)'s second-gradient model to different zones around the propagating crack, the rest of the structure obeying von Mises's standard first-gradient model. Figure 6 shows the zones considered in three different simulations. A calculation using Gologanu *et al.* (1997)'s model in the entire structure is also considered for reference.

The hypotheses and model parameters considered in all four computations are the same as those used for the simulation whose results were shown in red in Fig. 3.

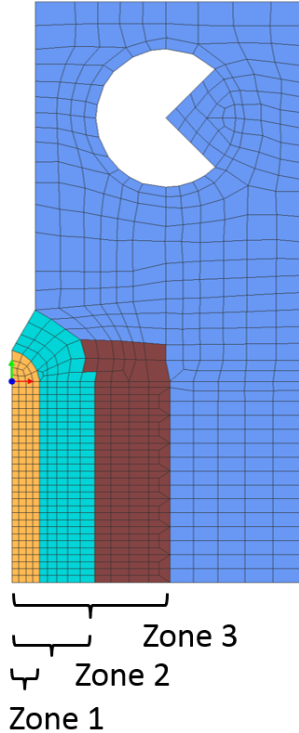


Fig. 6. Zones obeying Gologanu *et al.* (1997)’s second-gradient model in several simulations of the CT12 specimen.

Figure 7 compares the various load-displacement curves obtained and the corresponding CPU times.<sup>4 5</sup> The computation based on use of Gologanu *et al.* (1997)’s model everywhere being adopted as a reference, one sees that computations using this model only in Zones 2 or 3 of Fig. 6 yield very acceptable results, while requiring considerably less CPU time. (The gain is almost 50% if use of Gologanu *et al.* (1997)’s model is restricted to Zone 2). On the other hand the load-displacement curve obtained by using Gologanu *et al.* (1997)’s model in the smallest Zone 1 is somewhat inaccurate in its descending portion.

Instead of displaying “global” results like Fig. 7, Fig. 8 illustrates local features of the numerical solutions, in the form of the final distributions of the von Mises equivalent

<sup>4</sup> A slight “bump”, which was already visible though somewhat less conspicuously on the red curve of Fig. 3, is apparent near the maximum of all curves. No attempt has been made to reduce this bump. In all probability it arises from a somewhat inaccurate geometrical representation of the initial blunting of the crack (due to the use of simple triangular or quadrilateral elements), combined with a sudden acceleration of the development of damage when coalescence sets in. This bump could not be observed when using the GTN model, or when using Gologanu *et al.* (1997)’s model but without any coalescence, see Fig. 3. This is because for the GTN model, at the earlier instant when coalescence sets in, the crack is not seriously blunted yet; and for Gologanu *et al.* (1997)’s model without coalescence, because damage develops smoothly, without any sudden acceleration, throughout the whole mechanical history.

<sup>5</sup> The curve obtained by using Gologanu *et al.* (1997)’s model in the whole structure slightly differs from the red curve of Fig. 3, in spite of the identity of the model parameters employed. This is due to a small difference in the way boundary conditions are accounted for.

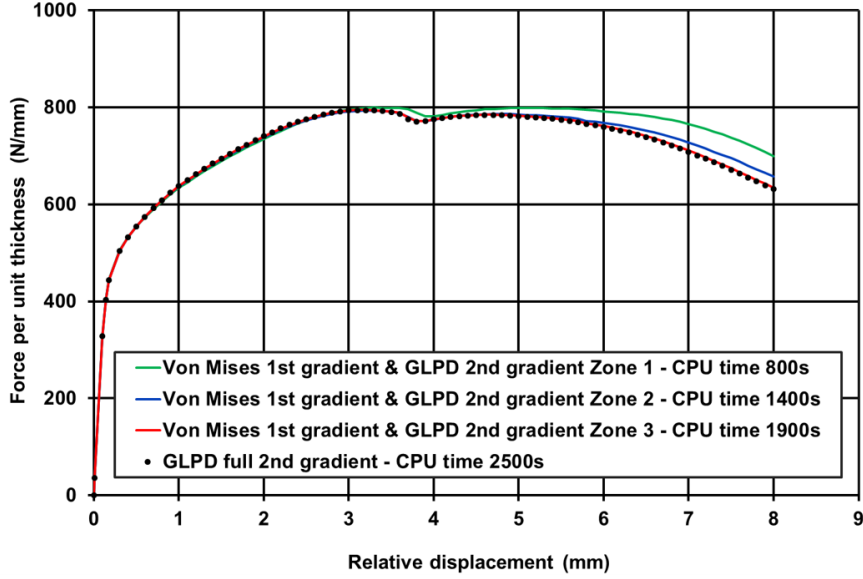


Fig. 7. Comparison of load-displacement curves of the CT12 specimen obtained by restricting the use of Gologanu *et al.* (1997)'s model to different zones.

stress, first in the simulation using Gologanu *et al.* (1997)'s model in the whole structure, second in that using this model only in Zone 1 of Fig. 6. There is little difference between the distributions found.

One notes however that in the latter simulation the von Mises stress is somewhat larger in the region lying just outside of Zone 1, on its right. This region obeys Gologanu *et al.* (1997)'s model in the first simulation and von Mises's standard one in the second. This suggests two possible explanations:

- The material is harder in the second simulation because von Mises's criterion disregards the impact of the porosity.
- In the first simulation, presence of the extra term  $\frac{1}{\sigma^2} \frac{Q^2}{b^2}$  in Gologanu *et al.* (1997)'s yield function induces a lowering of the magnitude of stress tensors satisfying the criterion. This effects persists even for vanishingly small porosities.

The very low values of the porosity in the region in question makes the first explanation less probable than the second. Anyway, this small lowering of the von Mises stress resulting from use of Gologanu *et al.* (1997)'s model is in all probability responsible for the slightly softer load-displacement curve obtained when using this model in the whole structure rather than in Zone 1 only, see Fig. 7.

#### 4 Numerical simulation of crack propagation in a bimetallic joint

The computations presented in this Section are much heavier and costlier than those depicted in the preceding Section, first because of the complex 3D geometry considered, second because the simulation of the propagation of the crack is pursued over a large distance. Their essential aim is to illustrate the practical applicability of Gologanu *et al.*

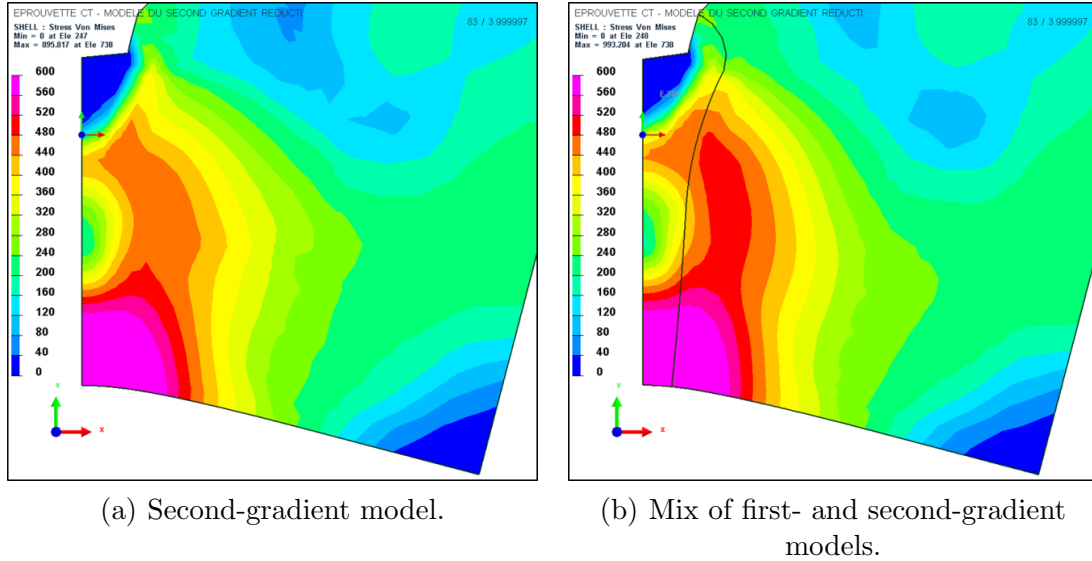


Fig. 8. Final distributions of the von Mises equivalent stress in the two types of simulations of the CT12 specimen.

(1997)'s second-gradient model even in a complex situation of industrial interest.

#### 4.1 Presentation of the problem

Dissimilar Metal Welds (DMWs) are common in the nuclear industry. Such DMWs connect components made of low-alloy steel on the one side and austenitic stainless steel on the other side. The fracture properties of DMWs have an important influence upon the toughness of the assembly and are therefore of major interest.

We consider here an experimental work of Mas and coworkers (Mas, 2014; Mas *et al.*, 2016a,b, 2018), devoted to an investigation of the microstructure and failure properties of an interface between a ferritic (18MND5) steel and a stainless (309L) steel, joined by a Submerged Arc Welding (SAW) process. This investigation included rupture tests in simple tension performed on flat notched specimens, which were extracted from a plate made of ferritic steel with a stainless cladding mimicking a DMW; the interface between the low-alloy and stainless steels (fusion line) was perpendicular to the direction of the load and located in the region of the notch, on or near the plane of minimum area. Figure 9 displays a photo of the vicinity of the notch and a schematic picture of the entire specimen.

Just after the deposition of the stainless layer by the SAW process, the metallurgical structure in the vicinity of the fusion line typically consisted of the following zones, encountered when moving from the low-alloy region to the stainless region:

- The low-alloy base metal (18MND5 steel), exhibiting a bainitic microstructure (mixture of laths of ferrite and  $\text{Fe}_3\text{C}$  carbide precipitates).
- A heat affected zone in the 18MND5 steel, stretching over 10 mm.
- A thin martensitic layer at the fusion line, of width varying between 5 and 200 microns.

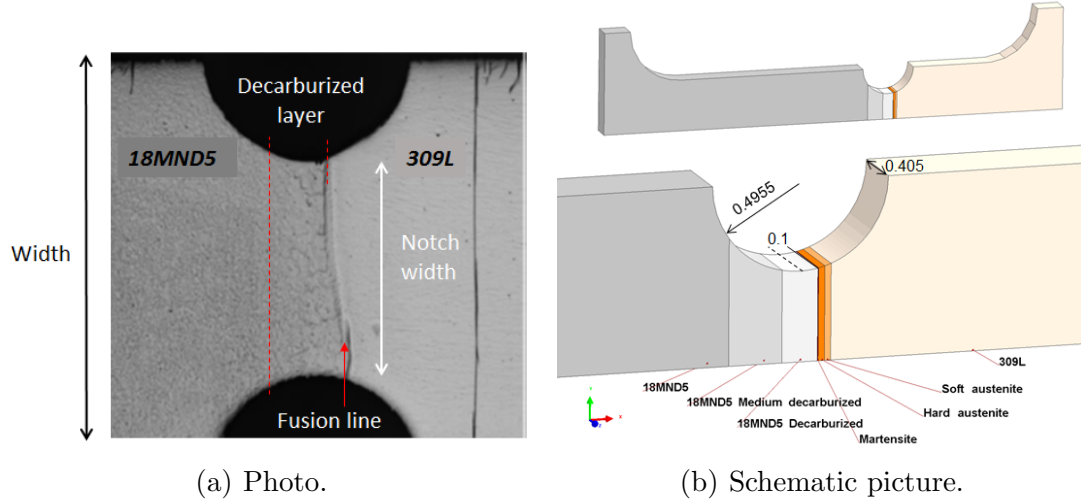


Fig. 9. Photo of the bimetallic specimen and schematic picture showing dimensions and metal-lurgical structures.

- On the stainless steel side, a fully austenitic zone of approximate width 70 microns.
- The stainless base metal (309L steel), exhibiting a mixed  $\delta + \gamma$  microstructure, with residual ferrite ( $\delta$ ) inclusions embedded within the austenitic ( $\gamma$ ) matrix.

After the cladding, a Post-Welding Heat Treatment (PWHT) was performed at a temperature of 610°C for 8 hours. (The practical aim of such a PWHT is to reduce the welding residual stresses in the DMW). This PWHT induced dissolution of carbides in the low-alloy steel and carbon diffusion from there to the stainless steel, resulting in the following modifications of the microstructure:

- Enlargement of ferritic grains, with very low carbon content and no carbides, in the low-alloy steel close to the fusion line; the nominal content of carbon being recovered only 500 microns away from the fusion line.
- Carbon enrichment of the martensitic and purely austenitic layers on the stainless steel side, with carbide precipitation taking place over a distance of 70 microns from the fusion line.

The final microstructure is illustrated in the photo of Fig. 9(a) and the schematic picture of Fig. 9(b).

In the numerical simulations, only half of the thickness and half of the height of the specimen need be meshed, thanks to symmetries. (Experimental crack paths are observed to at least approximately respect the natural geometrical symmetries). However the entire length must be meshed owing to the dissymmetric nature of DMWs. To represent the heterogeneous material properties, 7 zones are distinguished (Fig. 9(b)). The individual initial yield stress and hardening behaviour of each zone are determined on the basis of the experimental work of Mas (2014).

Two types of computations are performed, in which the zone labelled “18MND5 Decarburized” in Fig. 9 (where the crack is experimentally observed to propagate) is assumed to obey the GTN first-gradient model and Gologanu *et al.* (1997)’s second-gradient model,

respectively. The rest of the structure is assumed to obey von Mises’s standard model in both cases. The material parameters are very numerous, owing to the presence of 7 different zones, each with specific parameters; they may be found in Yang (2014)’s report. A few indications will suffice here: the values of the parameters governing coalescence are  $f_c = 1.05 \times 10^{-4}$ ,  $\delta = 6$  in the computation based on the GTN model, and  $f_c = 0.05$ ,  $\delta = 2$  in that based on Gologanu *et al.* (1997)’s model - note that the parameters for the former model promote an earlier and stronger porosity growth during coalescence; and the value of the microstructural distance  $b$  is 0.05 mm, much larger than the minimum element size of about 0.01 mm in the region of the crack.

#### 4.2 Load-displacement curves

Figure 10 compares the load-displacement curves obtained in the two computations to the experimental curve. Both computations yield quite acceptable results. However in the case of the GTN model such a good agreement is obtained at the expense of use of coalescence parameters ( $f_c = 1.05 \times 10^{-4}$ ,  $\delta = 6$ ) incompatible with theoretical estimates derived from FE simulations of elementary porous cells, see (Koplik and Needleman, 1988) and subsequent works; also, the critical porosity at the onset of coalescence is only 1.05 times larger than the initial porosity,  $f_0 = 10^{-4}$ , which is not reasonable since it means that coalescence sets in almost immediately. With Gologanu *et al.* (1997)’s model, a good agreement of numerical and experimental results is obtained with more reasonable coalescence parameters ( $f_c = 0.05$ ,  $\delta = 2$ ).

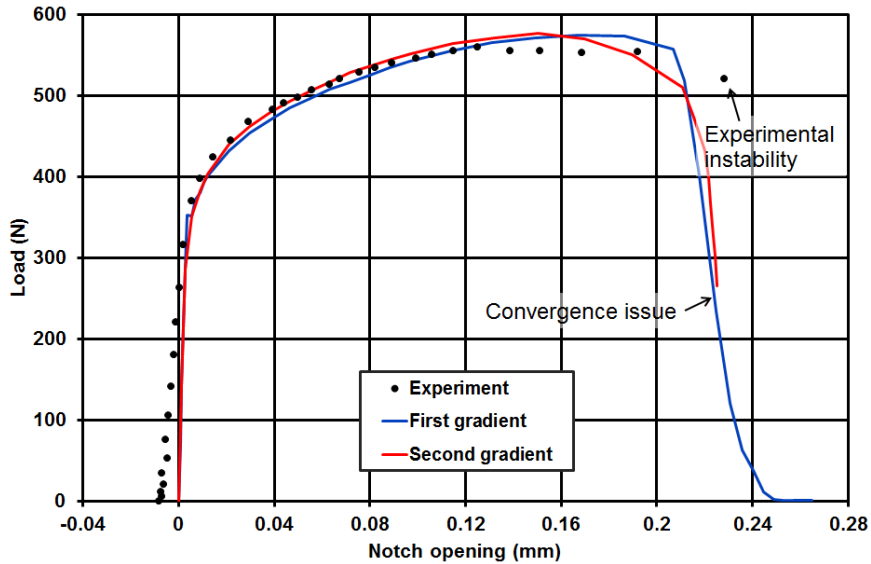


Fig. 10. Comparison of load-displacement curves of the bimetallic joint obtained with the GTN first-gradient model and Gologanu *et al.* (1997)’s second-gradient model.

Figure 10 shows that in the descending portion of the load-displacement curve, a convergence issue is encountered when Gologanu *et al.* (1997)’s model is used, in contrast to what occurs with the GTN model. This illustrates the (unsurprisingly) greater difficulty of obtaining convergence of the global elastoplastic iterations with Gologanu *et al.*

(1997)'s second-gradient model. But such a lack of convergence is not physically unreasonable in view of the experimental instability apparent at about the same value of the notch opening, see Fig. 10.

### 4.3 Fracture scenario

Figure 11 illustrates the final porosity distributions obtained in the two simulations, as observed on the external surface, and Fig. 12 does the same but with a view of the vertical plane of symmetry instead. These figures permit to observe the crack paths predicted.

Not only the final configurations of the crack, but also the sequence of its successive configurations, are quite different in the two computations:

- In the simulation using the GTN model, the crack initiates (the porosity starts to grow) at the centre of the notched section, at a distance in the deformed configuration of about 150 microns from the fusion line, in the decarburized zone (see the black arrow in Fig. 12(a)). It then extends toward the free surface. It gets closer to the fusion line while propagating but never actually reaches it, remaining at a minimum distance in the deformed configuration of about 40 microns (Figs. 11(a) and 12(a)).
- In the simulation using Gologanu *et al.* (1997)'s model, the crack initiates at the intersection of the cylindrical and planar free outer surfaces, on the fusion line (black arrow in Fig. 11(b)). It then propagates toward the interior of the specimen, in the decarburized zone. It remains stuck to the martensitic layer (Fig. 11(b)) except in the immediate vicinity of the central axis of symmetry, at the very end of its propagation (Fig. 12(b)).

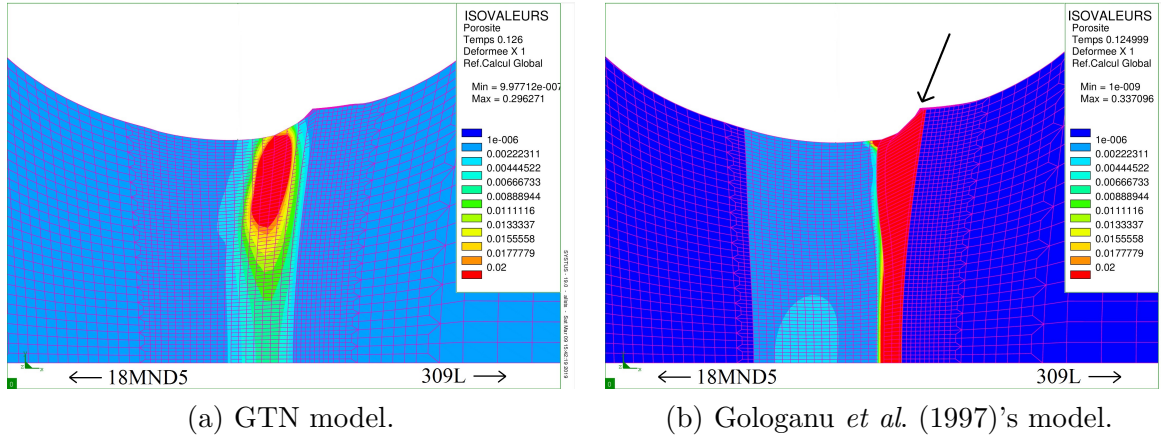


Fig. 11. Crack paths in the bimetallic joint - External view.

It is quite interesting that the two models yield such different fracture scenarios. Although neither of them fully agrees with Mas (2014)'s experimental observations, these observations tend to favour the predictions of Gologanu *et al.* (1997)'s model:

- Figure 13, borrowed and adapted from Mas (2014)'s work, shows the strain distribution (obtained by a digital image correlation technique) on the outer surface, close to the martensitic layer, at two early stages of crack propagation. The distribution is plotted

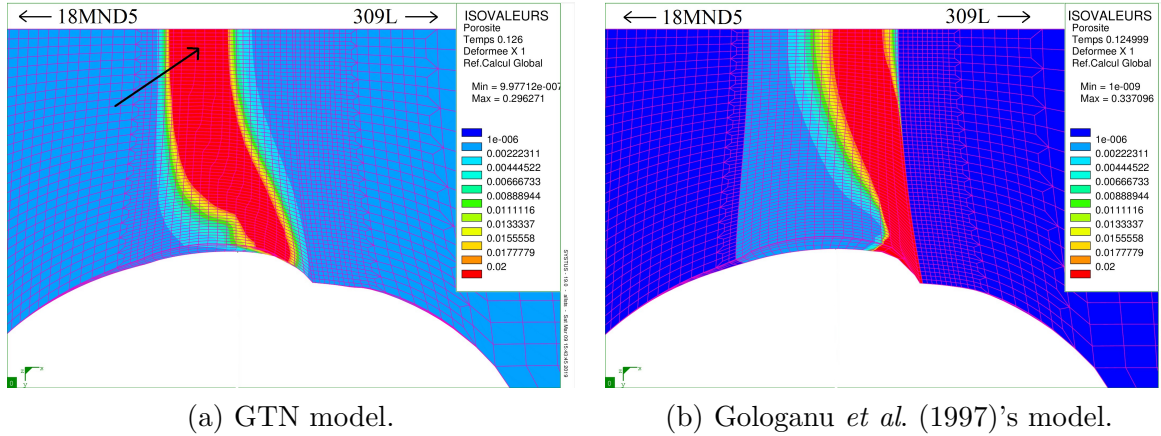


Fig. 12. Crack paths in the bimetallic joint - View of the plane of symmetry.

on the initial undeformed configuration. The maximum strain appears to occur at a distance from the martensitic layer not exceeding 20 or 30 microns, which suggests initial void growth on or very close to this layer. This observation is compatible with the predictions of Gologanu *et al.* (1997)'s model but not those of the GTN model, see above.

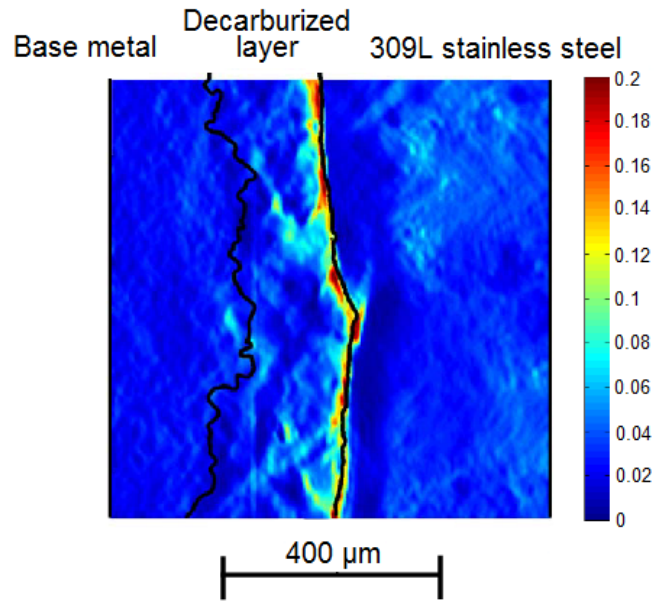
- Figure 14 shows a post-mortem micrograph of the vicinity of the fusion line. Although considerable void growth is observable very close to the martensitic layer, the final fracture occurs at a distance in the deformed configuration of about 60 microns from it, a layer of decarburized material remaining stuck to it; the distance from the final crack to the martensitic layer is therefore intermediary between those predicted by the two models.<sup>6</sup> (The prediction of Gologanu *et al.* (1997)'s model could very possibly be improved by modifying the value of the microstructural distance  $b$ , but this has not been attempted because of the length and cost of calculations).

## 5 Conclusion

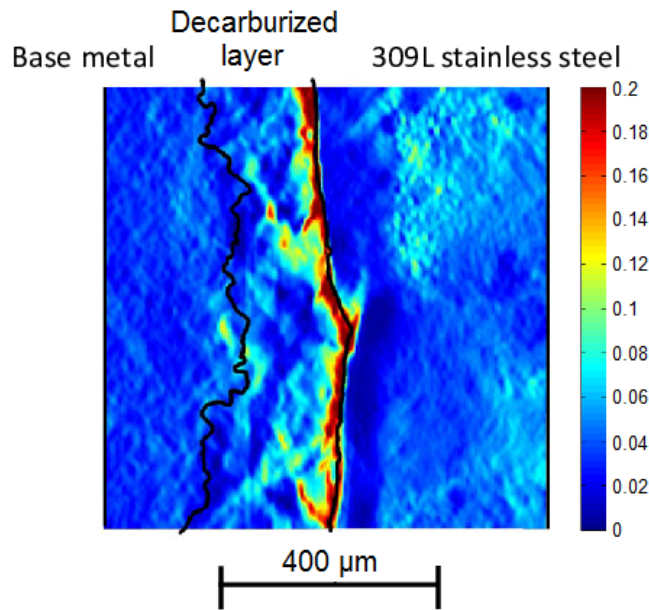
The purpose of this paper was to illustrate the practical applicability of Gologanu *et al.* (1997)'s second-gradient extension of the classical GTN model (Gurson, 1977; Tvergaard, 1981; Tvergaard and Needleman, 1984), aimed at solving the related issues of potentially unlimited localization of ductile damage and strain, and mesh-dependence in numerical FE computations.

Section 2 was first devoted to a presentation of Gologanu *et al.* (1997)'s model and Bergheau *et al.* (2014)'s corresponding numerical algorithm of solution. In the presentation of the numerical algorithm, emphasis was placed on Bergheau *et al.* (2014)'s original procedure of elimination of the additional nodal DOFs representing the components of the increment of strain between two successive instants of calculation. The aim was to show how this procedure, which reduces the nodal DOFs to the sole displacements like

<sup>6</sup> What is more, other observations show that this final crack does not originate from the region of maximum initial void growth; there is an effect of competition between two possible fracture loci, which escapes the predictions of both models.



(a) Overall stress 413 MPa.



(b) Overall stress 446 MPa.

Fig. 13. Strain distribution in the bimetallic joint at two early loading stages (after Mas (2014)).

for a standard first-gradient model, can be used to very easily mix elements obeying first- and second-gradient models. This kind of mix is highly convenient in practice in that it permits to use the second-gradient model only where it is really needed, that is in the damaged zone, thus leading to lighter and cheaper computations.

Section 3 then presented the results of several 2D simulations of rupture of a CT12 specimen made of a ductile stainless (SS 316L) steel, with a comparison with some experimental results of Marie (2000). These simulations used either the standard GTN first-gradient

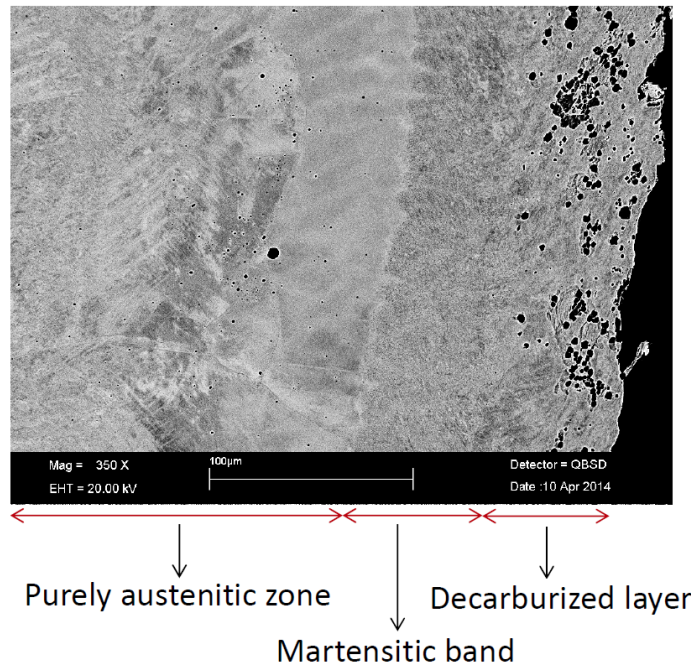


Fig. 14. Post-mortem micrograph of the vicinity of the fusion line.

model or Gologanu *et al.* (1997)'s second-gradient model, possibly restricted to a limited region around the propagating crack. The main conclusions were as follows:

- Use of Gologanu *et al.* (1997)'s model permits to get numerical predictions for the load-displacement curve agreeing closely with that recorded experimentally, using “reasonable” coalescence parameters agreeing acceptably with the theoretical values derived from micromechanical FE simulations of representative porous cells (Koplik and Needleman, 1988). Such good predictions could in all probability also be obtained with the GTN model, but at the expense of use of much lower values of the critical porosity at the onset of coalescence, disagreeing with Koplik and Needleman (1988)'s *ab initio* predictions.
- Using Gologanu *et al.* (1997)'s model only in a limited zone permits to reduce the CPU time by a factor of the order of 2, without degrading the quality of the results obtained, be they of global or local nature (load-displacement curve, stress distribution).

Finally Section 4.1 was devoted to much more complex and heavy 3D simulations of ductile rupture of a bimetallic (low-alloy/stainless) steel joint similar to those encountered in the nuclear industry, with reference to some experimental work of Mas and coworkers (Mas, 2014; Mas *et al.*, 2016a,b, 2018). Such computations were primarily intended as a demonstration that in spite of its sophistication, Gologanu *et al.* (1997)'s second-gradient extension of the GTN model may be used for FE simulations of propagation of cracks in ductile materials, in complex situations of industrial interest. But they also permitted to make some additional observations of interest:

- Again, satisfactory agreement of numerical predictions and experimental observations for the load-displacement curve can be obtained with both the GTN model and Golo-

ganu *et al.* (1997)'s model, but with much more reasonable values of the coalescence parameters when the latter model is used.

- The fracture scenarios predicted by the two models are markedly different. Mas (2014)'s experimental observations favour the predictions of Gologanu *et al.* (1997)'s model with regard to the locus of initial void growth. However none of the models fully captures the final experimental fracture locus.

## Acknowledgement

The authors wish to thank the FRAMATOME Company, and especially its Scientific Director Gilles Perrin, for its continued moral and financial support.

## References

- Bergheau J.M., Leblond J.B. and Perrin G. (2014). A new numerical implementation of a second-gradient model for plastic porous solids, with an application to the simulation of ductile rupture tests, *Comput. Meth. Appl. Mech. Engng.*, **268**, 105-125.
- Brosse A. (2009). Modélisation de déchirure ductile dans un tuyau inox - Calage des paramètres de Wilkins, *ESI France Internal Report F/LE/09/042/D/BPE* (in French).
- Enakoutsa K. (2007). Modèles non-locaux en rupture ductile des métaux, Ph.D. thesis, Université Pierre et Marie Curie (Paris VI) (in French).
- Enakoutsa K., Leblond J.B. and Perrin G. (2007). Numerical implementation and assessment of a phenomenological nonlocal model of ductile rupture, *Comput. Meth. Appl. Mech. Engng.*, **196**, 1946-1957.
- Enakoutsa K. and Leblond J.B. (2009). Numerical implementation and assessment of the GLPD micromorphic model of ductile rupture, *Eur. J. Mech. A/Solids*, **28**, 445-460.
- Gologanu M., Leblond J.B., Perrin G. and Devaux J. (1997). Recent extensions of Gurson's model for porous ductile metals, in: *Continuum Micromechanics*, P. Suquet, ed., CISM Courses and Lectures No. 377, Springer, pp. 61-130.
- Gurson A.L. (1977). Continuum theory of ductile rupture by void nucleation and growth: Part I - Yield criteria and flow rules for porous ductile media, *ASME J. Engng. Materials Technol.*, **99**, 2-15.
- Hill R. (1967). The essential structure of constitutive laws for metal composites and polycrystals, *J. Mech. Phys. Solids*, **15**, 79-95.
- Hughes T. (2000). *The finite element method: linear static and dynamic finite element analysis*, Dover Publications.
- Koplik J. and Needleman A. (1988). Void growth and coalescence in porous plastic solids, *Int. J. Solids Structures*, **24**, 835-853.
- Leblond J.B., Perrin G. and Devaux J. (1994). Bifurcation effects in ductile metals with nonlocal damage, *ASME J. Appl. Mech.*, **61**, 236-242.
- Mandel J. (1964). Contribution théorique à l'étude de l'érouissage et des lois d'écoulement plastique, in: *Proceedings of the 11th International Congress on Applied Mechanics*, Springer, pp. 502-509 (in French).
- Marie S. (2000). Méthodes de prédiction de grandes déchirures: données expérimentales nécessaires aux modélisations, *CEA Internal Report SEMT/LISN/RT/00-020* (in French).

- Mas F. (2014). Solidification and phase transformations in a dissimilar steel weld 18MND5/309L/308L: evolution of microstructure and mechanical properties, Ph.D. thesis, Université de Grenoble.
- Mas F., Martin G., Lhuissier P., Bréchet Y., Tassin C., Roch F., Todeschini P. and Simar A. (2016). Heterogeneities in local plastic flow behavior in a dissimilar weld between low-alloy steel and stainless steel, *Mater. Sci. Engng. A*, **667**, 156-170.
- Mas F., Tassin C., Roch F., Yescas M., Todeschini P. and Bréchet Y. (2018). Growth morphologies and primary solidification modes in a dissimilar weld between a low-alloy steel and an austenitic stainless steel, *Metals 2018*, **8**, 284, 21 pages.
- Mas F., Tassin C., Valle N., Robaut F., Charlot F., Yescas M., Roch F., Todeschini P. and Bréchet Y. (2016). Metallurgical characterization of coupled carbon diffusion and precipitation in dissimilar steel welds, *J. Mater. Sci.*, **51**, 4864-4879.
- SYSTUS User's Manual, ESI-Group.
- Tvergaard V. (1981). Influence of voids on shear band instabilities under plane strain conditions, *Int. J. Fracture*, **17**, 389-407.
- Tvergaard V. and Needleman A. (1984). Analysis of cup-cone fracture in a round tensile bar, *Acta Metall.*, **32**, 157-169.
- Yang J. (2014). Contribution à l'étude de la rupture ductile avec le modèle à gradient GLPD. *Research Report, ENSTA-ParisTech/ESI Group* (in French).

## A Appendix : Enforcement of the coincidence of $\Delta \mathbf{w}$ and $\Delta \boldsymbol{\epsilon}$ by a weak formulation

In Bergheau *et al.* (2014)'s approach, approximate coincidence of the variable  $\Delta \mathbf{w}$  and the increment of strain  $\Delta \boldsymbol{\epsilon}$  is enforced in a weak sense, using the shape functions associated to the nodes as test functions. This leads to the following condition at every node:

$$\int_{\Omega} N^p(\mathbf{x}) \Delta \mathbf{w}(\mathbf{x}) d\Omega = \int_{\Omega} N^p(\mathbf{x}) \Delta \boldsymbol{\epsilon}(\mathbf{x}) d\Omega \quad (\forall p).$$

The interpolation (10) of  $\Delta \mathbf{w}$  yields from there

$$\int_{\Omega} \sum_q N^p(\mathbf{x}) N^q(\mathbf{x}) \Delta \mathbf{w}^q d\Omega = \int_{\Omega} N^p(\mathbf{x}) \Delta \boldsymbol{\epsilon}(\mathbf{x}) d\Omega \quad (\forall p), \quad (\text{A.1})$$

or equivalently

$$\sum_q M^{pq} \Delta \mathbf{w}^q = \int_{\Omega} N^p(\mathbf{x}) \Delta \boldsymbol{\epsilon}(\mathbf{x}) d\Omega \quad (\forall p) \quad (\text{A.2})$$

where the quantities

$$M^{pq} \equiv \int_{\Omega} N^p(\mathbf{x}) N^q(\mathbf{x}) d\Omega \quad (\text{A.3})$$

are the components of a matrix  $\mathbf{M}$  analogous, except for the absence of the volumic mass, to mass matrices encountered in dynamic problems. Following the usual procedure for such problems - see for instance Hughes (2000) - this matrix may be ‘‘lumped’’, that is concentrated onto its diagonal by adding, for every line, all elements on this line and placing the result at the diagonal position.<sup>7</sup> The matrix  $\mathbf{M}$  is then replaced by a diagonal matrix  $\mathbf{M}_{\text{diag}}$  of diagonal components

$$M_{\text{diag}}^p \equiv \sum_q M^{pq} = \int_{\Omega} \left[ N^p(\mathbf{x}) \sum_q N^q(\mathbf{x}) \right] d\Omega = \int_{\Omega} N^p(\mathbf{x}) d\Omega \quad (\text{A.4})$$

where the relation  $\sum_q N^q(\mathbf{x}) = 1$  ( $\forall \mathbf{x}$ ) has been used. The system (A.2) on nodal values of  $\Delta \mathbf{w}$  then becomes:

$$M_{\text{diag}}^p \Delta \mathbf{w}^p = \int_{\Omega} N^p(\mathbf{x}) \Delta \boldsymbol{\epsilon}(\mathbf{x}) d\Omega \quad \Rightarrow \quad \Delta \mathbf{w}^p = \frac{1}{M_{\text{diag}}^p} \int_{\Omega} N^p(\mathbf{x}) \Delta \boldsymbol{\epsilon}(\mathbf{x}) d\Omega \quad (\forall p). \quad (\text{A.5})$$

Since  $\Delta \boldsymbol{\epsilon}(\mathbf{x})$  may be expressed, thanks to equation (9), as a function of the nodal values of  $\Delta \mathbf{u}$ , equation (A.5) provides explicit expressions of all nodal values of  $\Delta \mathbf{w}$  in terms of those of  $\Delta \mathbf{u}$ . This leads to equation (12) of the text.

<sup>7</sup> This is equivalent to using, in equation (A.1), the approximation  $\Delta \mathbf{w}^q \simeq \Delta \mathbf{w}^p$  for all pairs  $(p, q)$  such that  $\int_{\Omega} N^p(\mathbf{x}) N^q(\mathbf{x}) d\Omega \neq 0$ , that is all pairs of neighbour nodes. This approximation is justified for sufficiently refined meshes.

## B Appendix : Material parameters for the simulations of Section 3

In the following table  $E$  denotes Young's modulus,  $\nu$  Poisson's ratio,  $\sigma_0$  the initial yield stress,  $q$  Tvergaard (1981)'s parameter,  $f_0$  the initial porosity,  $A_I$  and  $A_{II}$  parameters pertaining to the quadratic form  $Q^2$  (see Subsection 2.1 and the work of Bergheau *et al.* (2014)), and  $b$  the microstructural distance appearing in the yield criterion (3).

$E$ (MPa)	$\nu$	$\sigma_0$ (MPa)	Hardening law	$q$	$f_0$	$A_I$	$A_{II}$	$b$ (mm)
203,000	0.3	165.3	See below	1.47	0.0008	0.194	6.108	0.5
Equivalent plastic strain			0	0.00006	0.00019	0.00122	0.00327	0.01378
Yield stress (MPa)			165.3	185.3	195.3	225.4	245.9	284
0.02419	0.05376	0.09315	0.12482	0.15553	0.18534	0.21433	0.24245	0.28326
307.4	364.1	429.3	477.2	521.4	561.4	597.8	631.6	676.6
0.39584	0.49527	0.64452	0.74407	0.89346	0.94326	0.99308	1.3904	2
784.3	866.1	973.4	1037.4	1125.1	1152.5	1179.1	1369.2	1600